

Survivability of copper projectiles during hypervelocity impacts in porous ice: A laboratory investigation of the survivability of projectiles impacting comets or other bodies



K.H. McDermott, M.C. Price, M. Cole, M.J. Burchell*

Centre for Astrophysics and Planetary Science, School of Physical Sciences, University of Kent, Canterbury, Kent CT2 7NH, United Kingdom

ARTICLE INFO

Article history:

Received 27 October 2014

Revised 4 December 2015

Accepted 11 December 2015

Available online 6 January 2016

Keywords:

Impact processes

Cratering

Mars

Meteorites

Comet Tempel-1

ABSTRACT

During hypervelocity impact ($> a \text{ few km s}^{-1}$) the resulting cratering and/or disruption of the target body often outweighs interest on the outcome of the projectile material, with the majority of projectiles assumed to be vaporised. However, on Earth, fragments, often metallic, have been recovered from impact sites, meaning that metallic projectile fragments may survive a hypervelocity impact and still exist within the wall, floor and/or ejecta of the impact crater post-impact. The discovery of the remnant impactor composition within the craters of asteroids, planets and comets could provide further information regarding the impact history of a body. Accordingly, we study in the laboratory the survivability of 1 and 2 mm diameter copper projectiles fired onto ice at speeds between 1.00 and 7.05 km s^{-1} . The projectile was recovered intact at speeds up to 1.50 km s^{-1} , with no ductile deformation, but some surface pitting was observed. At 2.39 km s^{-1} , the projectile showed increasing ductile deformation and broke into two parts. Above velocities of 2.60 km s^{-1} increasing numbers of projectile fragments were identified post impact, with the mean size of the fragments decreasing with increasing impact velocity. The decrease in size also corresponds with an increase in the number of projectile fragments recovered, as with increasing shock pressure the projectile material is more intensely disrupted, producing smaller and more numerous fragments. The damage to the projectile is divided into four classes with increasing speed and shock pressure: (1) minimal damage, (2) ductile deformation, start of break up, (3) increasing fragmentation, and (4) complete fragmentation. The implications of such behaviour is considered for specific examples of impacts of metallic impactors onto Solar System bodies, including LCROSS impacting the Moon, iron meteorites onto Mars and NASA's "Deep Impact" mission where a spacecraft impacted a comet.

© 2016 The Authors. Published by Elsevier Inc. This is an open access article under the CC BY license (<http://creativecommons.org/licenses/by/4.0/>).

1. Introduction

Hypervelocity impacts occur in the Solar System when two bodies collide at speeds in excess of a few km s^{-1} . Typical impact speeds depend on the location in the Solar System, along with the precise details of the relative orbits of the respective bodies (either around the Sun or other nearby body) and their mutual gravitational influence. In the inner Solar System impacts on the Earth are typically described as being at 20 or 25 km s^{-1} , but are actually usually distributed over a wide range of speeds with the quoted values being the modal impact speed (e.g., see Fig. 4 in [Le Feuvre and Wicczorek, 2011](#)). In the outer Solar System impact speeds are generally lower, unless in the gravitational potential

of a giant planet (e.g., see [Dell'Oro et al., 2001](#); [Zahnle et al., 2003](#); [Burchell et al., 2005](#); [Burchell, 2012](#)). Mean collision speeds in the asteroid belt for example are approximately 5 km s^{-1} , falling to around 1 km s^{-1} in the vicinity of Pluto. For comets, which spend most of their life in the outer Solar System, mean impact speeds will be in the range of 0.5 to a few km s^{-1} . The results of high speed impacts are widely studied, with most studies focusing on the fate of the target, i.e., does a crater result or, if the energy density is sufficient, will the target break apart in a catastrophic disruption?

The fate of the impactor however, is not as extensively studied compared to the growth of the resulting crater. Indeed as stated in [Yue et al. \(2013\)](#), it is often assumed that, especially in larger impacts, the projectile has melted or vaporised so that, at best, only small fragments survive. Thus the projectile fate is a relatively neglected field of study. There are some exceptions to this, such

* Corresponding author.

E-mail address: m.j.burchell@kent.ac.uk (M.J. Burchell).

as work by Hernandez et al. (2006), Kenkmann et al. (2013) and Ebert et al. (2014) which investigated the processes that occur between the target and projectile during hypervelocity impacts. Or, for example, by Bowden et al. (2008) and Parnell et al. (2010) who looked for survival of biomarkers in projectile fragments which survived impacts, and Burchell et al. (2014a) who looked for transfer of volatiles to targets after impacts. Indeed, survival of diatom fossils has been shown in projectile fragments in laboratory experiments (Burchell et al., 2014b). Survival of the projectile in laboratory experiments as it impacts porous silicates and ice also has been reported, with around 20% of the impactor recovered after impacts in porous ice at $\sim 5 \text{ km s}^{-1}$ (Daly and Schultz, 2013) and up to 75% survival after impacts into powdered pumice (Daly and Schultz, 2014). Schultz and Gault (1984) linked projectile deformation and fragmentation in low speed impacts ($< 4 \text{ km s}^{-1}$) to the crater-size scaling relationship as well as the resulting crater morphology. There is also discussion in the literature as to where material survives after impact in sub-surface regions (which if icy can later be exposed, e.g., see Daly and Schultz, 2015). There are thus many reasons why the fate of the projectile after impact is significant.

However, as stated earlier, after an impact, it is often the resulting crater that is the focus of the research, rather than the projectile. Certainly this is the case if the large scale effects of the impact are being considered (e.g., cratering or catastrophic disruption), but in some cases it is the projectile material that is of interest. This is commented on by Daly and Schultz (2013). Indeed, a recent review of terrestrial impact structures shows that, in around 50 of the 180 or so known impact craters on Earth, geochemical means can be used to find traces of projectile material via modified elemental abundances or isotope ratios (Goderis et al., 2013). Indeed, in 13 cases, projectile fragments (usually metallic) have been recovered at terrestrial impact sites (Table 15.1, Goderis et al., 2013). Most of the craters which have yielded fragments are small (most of the craters being less than 1 km in diameter) and young (most are less than 1 million years old), although as noted below, this is not always the case. That the material is mostly found in small craters is not a surprise, as the impactors, being correspondingly at the small end of the size spectrum, will have been slowed somewhat as they entered the Earth's atmosphere, reducing the impact speed and thus reducing the chance of partial melting or vaporisation. Similarly, being metallic implies a greater strength than for a rocky body, again increasing the chance of survival (although non-metallic materials can also survive). Projectile fragments have however, also been recovered from larger craters with ages of order 100 million years (e.g., Chixulub crater, 64.98 ± 0.05 million years old and Morokweng crater, 145.0 ± 0.8 million years old, see Goderis et al., 2013).

Further afield, recent analysis of Apollo era lunar samples shows that projectile fragments arising from impacts early in its history can be found within the near surface environment (regolith) of the Moon (e.g., Joy et al., 2012 and references therein). Looking further afield, the dark material recorded on the asteroid Vesta is thought to be the remnants of the Veneneia basin low velocity ($< 2 \text{ km s}^{-1}$) impact by a carbonaceous chondritic body (Reddy et al., 2012). The possibility of successful transfer of material to Vesta in impacts has been considered experimentally by Daly and Schultz (2014) whose laboratory experiments firing projectiles into powdered pumice transfer significant amounts of material to the target. Recent work has identified that lithological projectile material can survive impacts at speeds of up to 960 m s^{-1} (Nagaoka et al., 2014), and it has been proposed (Yue et al., 2013) that even in impacts at 12 km s^{-1} , mineralic impactor material (dunite in their simulation) may survive, and be found in impact craters on bodies such as the Moon (also see Schultz and Crawford, 2014). There are also examples of non-indigenous mate-

rials found inside meteorites (e.g., Zolensky et al., 1996; Gounelle et al., 2003) suggesting successful transfer of impactor to target.

We also note the observation of iron meteorites on Mars (e.g., see Arvidson et al., 2011 and Fairen et al., 2011, and references therein). These are of sizes 30–60 cm and indicate the arrival at Mars of metallic impactors. Depending on the density of the martian atmosphere when such bodies arrived, they do not have to be much larger in order to pass through the atmosphere with little deceleration and to impact the surface at high speed in a cratering type event.

There is thus no reason to suppose that projectile fragments are not present in, or around, many impact craters across the Solar System. Indeed, there are also a few specific cases of man-made impacts on Solar System bodies (such as SMART-1, Lunar Prospector, and LRO which have impacted the Moon). Further out in the Solar System, the *Deep Impact* mission was the first mission to investigate the composition of a comet using a projectile (a spacecraft of 364 kg, 49% of which was porous copper, with another 6.5 kg of un-used hydrazine) which impacted Comet 9P/Tempel-1 at 10.3 km s^{-1} to excavate an impact crater (A'Hearn et al., 2005; Veverka et al., 2013). The impact also created an impact light flash and ejecta plume, both of which were studied by the accompanying spacecraft (see Ernst and Schultz, 2007 for a discussion of the light flash). The behaviour of the material ejected from the impact suggested that the comet nucleus had a bulk density of 400 kg m^{-3} , albeit with a large uncertainty ranging from 200 to 1000 kg m^{-3} (Richardson et al., 2007 who looked at the ejecta flow), compared to Schultz et al. (2007) who estimated the near surface density to be $200\text{--}500 \text{ kg m}^{-3}$ based on crater growth. The resultant impact crater was not observed by the original mission spacecraft, but was observed by a later fly-by of NASA's *Stardust* spacecraft (Veverka et al., 2013). This later mission reported that the crater-like feature at the impact site was some $49 \pm 12 \text{ m}$ across, implying an ejected mass of $1.6 \times 10^6 \text{ kg}$ with a range of $5.4 \times 10^5\text{--}2.6 \times 10^6 \text{ kg}$ (Richardson and Melosh, 2013), although estimates of the ejected mass from Earth-based observers go as high as $8 \times 10^6 \text{ kg}$ (indeed this latter estimate refers only to the fraction of ejected material which left the gravity field). There is a discussion of this discrepancy in Schultz et al. (2007, 2013) and the larger amount of ejected material seems to suggest a larger crater than originally predicted. Separate analyses have suggested that the original, transient crater had a diameter of $200 \pm 20 \text{ m}$, which then collapsed and/or eroded, or alternatively that the presently observed crater of order 50 m diameter is the central crater of a nested crater structure, which resembles an inverted sombrero, rather than the classic simple bowl-shaped crater with a well-defined rim wall 180 m in diameter (see Schultz et al., 2007 and 2013 for a discussion of relevant impact mechanics and observations from *Stardust*-NExT).

In previous papers (Burchell and Johnson, 2005; Burchell et al., 2005) we reported on crater size for impacts of projectiles onto solid ice targets. Given that the *Deep Impact* mission target was not expected to be solid (and indeed the results were compatible with an impact in a highly porous surface material), in Burchell and Johnson (2005) the results were extrapolated to the *Deep Impact* case, allowing for target porosity, and predicted a crater of diameter 50–150 m and crater volume estimate of 4877 m^3 for a solid ice target, implying an excavated mass of some $4.5 \times 10^6 \text{ kg}$. If the ice target was porous, Burchell and Johnson (2005) point out that their modelling indicates that whilst parameters such as crater depth (and hence volume) would increase, the amount of actual ice excavated varies by much less. Some of this excavated mass will have gone into any raised rim wall around a crater, but as pointed out in Burchell and Johnson (2005), some will also be present as a fully compacted ice mass beneath the crater. No attempt was made in that work to estimate the amount of

icy material which flowed as ejecta rather than being simply displaced, but applying a crude value of $\sim 50\%$ reduces the amount of ice available to be ejecta to some 2.25×10^6 kg, close to the mean estimate of Richardson and Melosh (2013) and within their upper bound on the ejecta mass. The fate of the copper projectile was however, still uncertain.

Given that there is clearly evidence of survival of metallic impactor material at terrestrial impact sites (e.g., see Goderis et al., 2013), plus various examples of projectile material on other Solar System bodies, and that there is indeed the specific example of a man-made impact of a predominantly copper projectile on a comet (Tempel-1), we have conducted a study of the survival of copper projectiles in high speed impacts on porous ice. This study uses copper projectiles of 1–2 mm diameter, fired at porous ice targets (porosity ≈ 0.53) with impact speeds in the range $1.00\text{--}7.05$ km s $^{-1}$. Whilst the upper speed used here is lower than that in the *Deep Impact* mission to comet 91P/Tempel-1, it permits a reasonable extrapolation to that particular case. This however uses a solid copper projectile in the laboratory experiments, whereas the real spacecraft was a more complicated object, being some 49% copper, 25% aluminium with the balance of the mass comprising spacecraft systems (antennas, etc.) and containing various void space (with milled copper in order to reduce the effective density). In addition, the experiments reported here involved impacts at normal incidence, whereas the *Deep Impact* mission involved an impact at 30° from the horizontal.

2. Method

In this work, nineteen high speed impact experiments were undertaken using the two stage light gas gun (LGG) at the University of Kent (Burchell et al., 1999) in order to investigate the survivability of copper (Cu) projectiles when fired at a range of hypervelocity speeds ($1.00\text{--}7.03$ km s $^{-1}$) into porous ice at normal incidence. Projectile speeds were measured in-flight to better than 1% by passage of the projectile between two light curtains. Given that the target chamber was evacuated to ~ 10 mbar during a shot, there was no significant deceleration of the projectiles in flight pre-impact. The targets were made of flaked ice, with a typical crystal size between 1 and 3 mm, with porosity (density of target/density of solid ice) of 0.53 ± 0.02 (based on measurement of each target, and where the error given is the standard deviation of the individual samples about the mean). During the shot the target was placed in a target chamber cooled using a liquid nitrogen cold plate which allowed the target to be kept at approximately 255 ± 3 K at the point of impact. One projectile was fired per shot. The projectiles were either 1 mm or 2 mm diameter copper spheres, supplied by Salem Speciality Ball Co., USA (Fig. 1a and b) which were intended to act as a proxy for the *Deep Impact* impactor. The projectiles were manufacturer's grade 200, i.e., dimensions were accurate to within 0.001 in. (0.025 mm).

Post-shot the target was excavated around the crater site. In cases where the projectile was intact it was extracted by hand from beneath the crater. If the projectile broke up, the ice around the

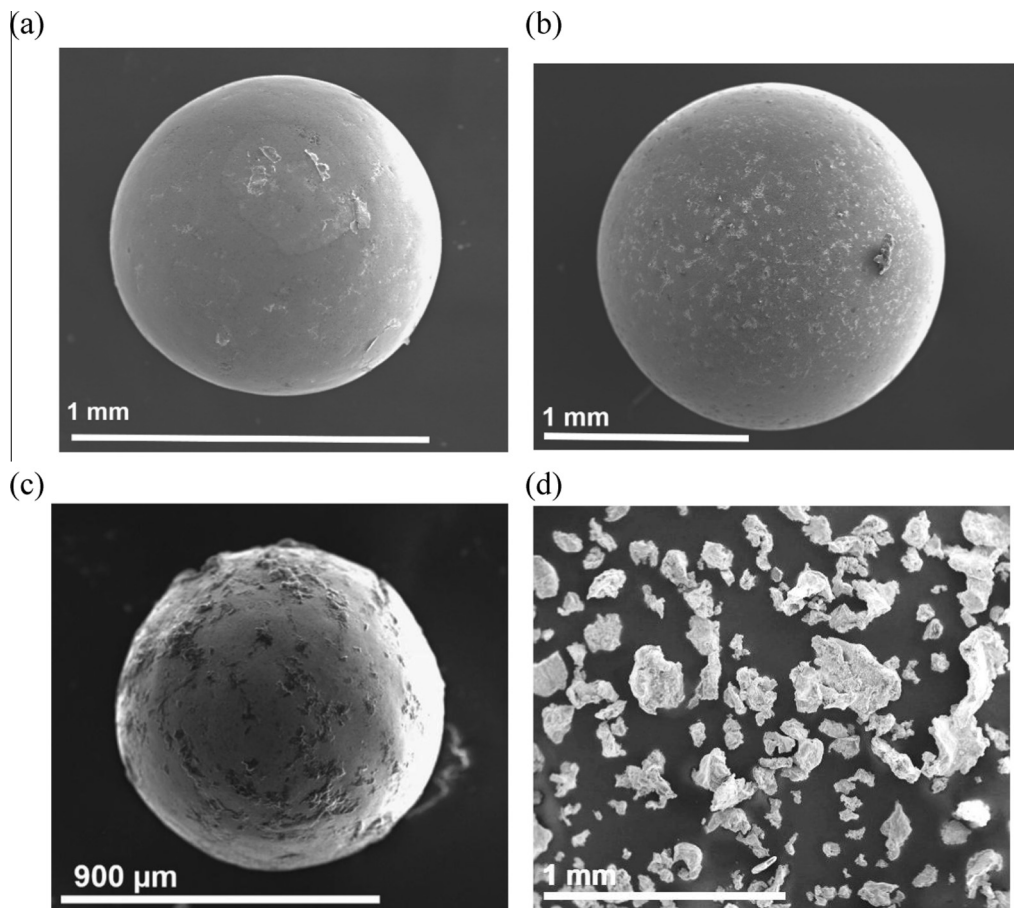


Fig. 1. Secondary electron images (20 kV) of projectiles before and after impact. (a) Projectile pre-shot (1 mm diameter), (b) projectile pre-shot (2 mm diameter), (c) example of 1 mm diameter copper projectile (shot number G030702#2) collected after impact at 1.12 km s $^{-1}$ showing the uneven surface features compared to an un-shot standard (b), and (d) projectile fragments collected after a 2 mm Cu projectile was fired into porous ice at 5.97 km s $^{-1}$ (shot number G121002#2).

crater was removed with the Cu projectile embedded within, and then left to melt. The melt water was then filtered to collect the Cu projectile fragments. In all cases the collected copper material was then observed and measured using optical microscopy and scanning electron microscopy. The scanning electron microscope used to observe and measure the Cu fragments was a Hitachi S3400N. All the images were obtained without a carbon coating, using an operating voltage of 20 kV. An Oxford Instruments EDX system (XMAX-80 silicon drift detector) was used (calibrated against a Cobalt standard), to determine the composition of the fragments, as carbon material from the gun could have become mixed in with the Cu fragments. The fragment sizes were measured using the Oxford Instruments' 'INCA' software. The given length indicates the longest axis of the grains and the width is the size of the grain perpendicular to the longest axis. Each grain was measured once and a statistical analysis determined the range, mean, etc. of the Cu fragments. Difficulty in transferring material from the filter paper to the SEM, set the lower size limit on fragments of around 50 μm .

3. Results

Table 1 shows the key variables in each shot, including the kinetic energy of each projectile and the estimated peak impact shock pressure. The peak pressures were calculated using the Planar Impact Approximation (Melosh, 1989). This assumes a linear wave speed equation for both ice and copper and that the projectile hit a solid ice target (i.e., no allowance is made for the porosity of the target). This latter assumption is considered reasonable, as only a peak pressure is being found, not the full pressure history of an impact vs. time.

Additionally, we used Ansys' AUTODYN (Hayhurst and Clegg, 1997) hydrocode to determine the peak pressures experienced within the projectile. Due to the simple normal incidence impact geometry, all simulations were modelled in 2-dimensions using a Lagrangian method, with 10 cells across the radius of the projectile (giving a total of $\sim 500,000$ cells in total). Standard AUTODYN

library materials were used to simulate copper (Steinberg, 1991 for EoS data using a strength model from Steinberg et al., 1980). Ice was simulated using the 5-phase EoS detailed in Senft and Stewart (2008), using an easy to implement strength model validated against experimental data described in Fendyke et al. (2013). Peak pressures were determined by placing tracers (referred to as 'gauges' in AUTODYN) within the projectile. The peak pressures experienced (the maximum, median and minimum) within the projectile during the impacts for shots are given in Table 2. The maximum simulated peak pressures are similar to those found by using the PIA within typically 10–20%, giving additional confidence that the pressures calculated using either method are robust. However, the use of the hydrocode allows us to consider the range of peak pressures experienced across the bulk of the projectile. We find that the median peak pressure was typically just over one third of the maximum value, and the minimum peak pressure to which any part of the projectile was shocked was typically less than 10% of the maximum value. The ability of hydrocodes to correctly produce peak pressures is discussed for example in Pierazzo et al. (2008), where it is suggested that if, as here, 10 cells are used across a projectile, then with an appropriate EoS, pressures should be accurate to better than 10%.

The number of collected fragments and their mean size post shot from each impact experiment are displayed in Table 1. For both 1 mm and 2 mm diameter projectiles, all shots with an impact speed of $< 2 \text{ km s}^{-1}$ caused no breakup of the projectile with the whole spherical projectile being easily recovered from the target. However, whilst intact, the surface of these projectiles showed evidence of cracking and pitting of the surface (Fig. 1c). At shot speeds greater than 2 km s^{-1} (equivalent to a peak pressure of 6.8 GPa calculated with the PIA) the impact results in the fragmentation and disruption of the Cu projectiles for both 1 mm and 2 mm spheres (examples of the fragments collected after impact are shown in Figs. 1d and 2). Fig. 3 shows the relationship between the number of projectile fragments collected (n) and the shot speed (v , Fig. 3a) and peak pressure (P , Fig. 3b). When fitting the data, if fitted separately the results for both the 1 mm and 2 mm diameter projectiles were similar, suggesting that size differences at this range have no

Table 1

The impact variables for each shot. Peak pressure was calculated using the Planar Impact Approximation, which uses a linear wave speed equation with c (m s^{-1}) and S values for solid ice of 1280 and 1.56 with density 910 kg m^{-3} (Melosh, 1989), and copper of 3982 and 1.46 with density 8940 kg m^{-3} (Ahrens and Johnson, 1995). In a few shots some measurements were not made and are entered as blanks in the table (e.g., we failed to find the projectile post-shot or some fragments were lost during analysis). The uncertainty on the fragment size is given by the standard deviation in the mean. Where only one fragment was recovered, i.e., the original projectile intact, there is no uncertainty given on fragment length as in these cases this was determined by the measurement error which was approximately 5 μm in these cases.

Shot #	Diameter (mm)	Speed (km s^{-1})	Kinetic energy (J)	Peak pressure (GPa)	Number of fragments post shot	Mean fragment length (μm) ^a	Mass fraction recovered post shot
G081105#2	1	1.07	2.46	2.58	1	–	–
G030702#2	1	1.12	2.70	2.76	1	980	0.99
G090702#3	1	1.16	2.89	2.92	1	930	1.00
G090702#1	1	1.28	3.52	3.39	1	1020	0.99
G051202#1	1	2.39	12.3	9.10	2	1090 \pm 710	0.78
G291104#1	1	3.44	25.4	16.6	31	240 \pm 140	0.17
G291104#3	1	3.74	30.1	19.1	12	230 \pm 140	–
G111202#1	1	4.76	48.7	28.7	13	230 \pm 150	–
G240205#3	1	5.07	55.3	32.0	73	62 \pm 32	0.07
G070305#1	1	5.07	55.3	32.0	35	61 \pm 42	–
G100103#1	1	7.05	116	56.7	–	–	–
G081002#1	2	1.16	24.8	2.92	1	2010	1.00
G081002#2	2	1.20	26.5	3.07	1	2020	1.00
G250603#1	2	2.60	124	10.4	4	1900 \pm 630	0.69
G300902#1	2	2.86	151	12.2	12	1020 \pm 690	0.60
G011002#1	2	3.10	177	14.0	22	900 \pm 450	0.62
G210614#1	2	4.23	330	23.5	239	330 \pm 230	0.69
G121002#1	2	5.97	656	42.4	584	130 \pm 80	0.08
G270603#1	2	6.30	731	46.6	431	160 \pm 140	0.26

^a Where values exceed 100 they have been rounded to the nearest 10 with no significant loss of accuracy.

Table 2

Peak pressures as modelled using Ansys' AUTODYN hydrocode. Columns refer to the maximum peak pressure experienced anywhere within the projectile, the median peak pressure and the minimum peak pressure.

Velocity (km s ⁻¹)	Peak pressure (Max) GPa	Peak pressure (Median) GPa	Peak pressure (Min) GPa
1.00	2.03	0.42	0.18
2.39	7.18	2.39	0.51
3.74	16.3	5.86	0.82
4.76	25.3	9.83	3.56
7.05	52.1	22.5	6.80
8.50	72.9	33.1	6.92
10.0	96.7	46.5	9.85

significant effect on the degree of fragmentation the projectile material experienced during the impacts. We excluded from the fits the shots below 2 km s⁻¹, as they have not fragmented. We fitted the combined dataset (i.e., 1 and 2 mm together) with both linear and power law fits. The results were:

$$n = -(330 \pm 136) + (110 \pm 32)v, \quad r = 0.7081 \quad (1)$$

$$n = (0.008 \pm 0.029)v^{(6.01 \pm 1.97)}, \quad r = 0.8401 \quad (2)$$

and,

$$n = -(165 \pm 83) + (12.0 \pm 3.1)P, \quad r = 0.7481 \quad (3)$$

$$n = (0.00088 \pm 0.0038)P^{(3.46 \pm 1.13)}, \quad r = 0.8395 \quad (4)$$

where r is the regression coefficient of the fit, v is in km s⁻¹ and P in GPa.

When considering the size of the fragments we use the mean fragment size. This is suitable for a normal distribution of the fragment size data set. However here, fragmentation (similar to grinding) produces a log-normal distribution producing a skewed distribution in favour of the smaller fragment sizes. In such cases the mode average may provide a more accurate average approximation for the fragment size data set. Accordingly, we calculated the mode in each case, but found that it was only slightly reduced from the mean (typically a 5–10% reduction with the smaller difference at higher speeds where there are more data). We therefore use the more common mean value in our analysis. Accordingly, in Fig. 4 we show the mean fragment size (S) vs. the shot speed (v , Fig. 4a) and peak pressure (P , Fig. 4b). We fit the data with power law fits to each data set (1 mm and 2 mm) separately (note that again we excluded from the fits data from the shots with impacts speeds less than 2 km s⁻¹, as they have not fragmented). We find:

$$S = (22,456 \pm 8867)v^{-(3.49 \pm 0.42)}, \quad (1 \text{ mm}), \quad r = -0.9856 \quad (5)$$

$$S = (90,579 \pm 64,773)v^{-(4.11 \pm 0.71)}, \quad (2 \text{ mm}), \quad r = -0.979 \quad (6)$$

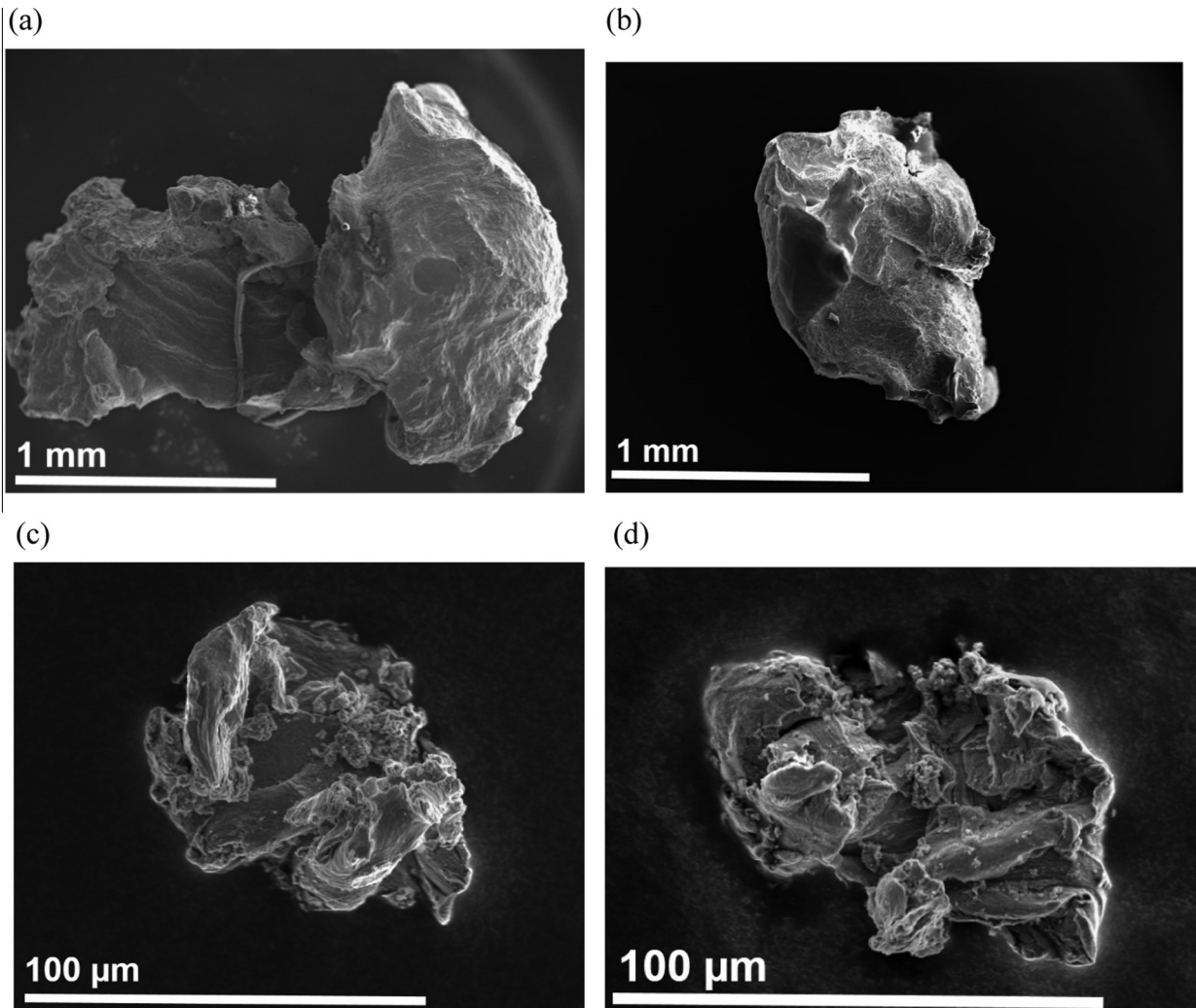


Fig. 2. Secondary electron images (20 kV) of post shot Cu projectile fragments from (pre-shot) 2 mm diameter spheres: (a) 2.60 km s⁻¹ (shot number G250603#1), (b) 3.10 km s⁻¹ (shot number G011002#1), (c) 5.97 km s⁻¹ (shot number G121002#1), and (d) 6.30 km s⁻¹ (shot number G270603#1). (Note that in each case the image brightness has been enhanced to make the surface detail clearer.)

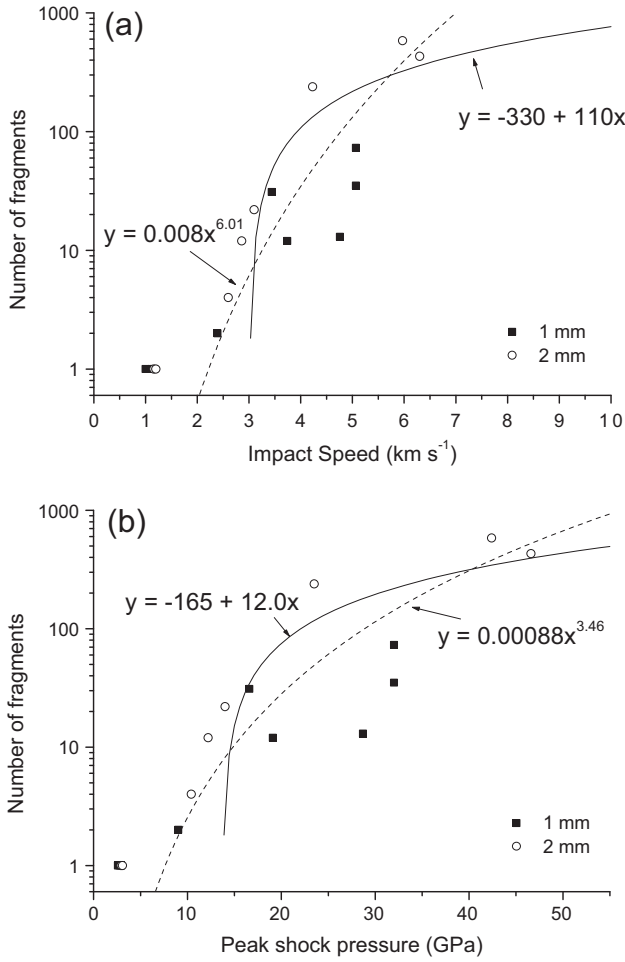


Fig. 3. The number of projectile fragments collected vs. (a) impact speed and (b) peak pressure corresponding to each speed. Black squares represent 1 mm projectiles, circles represent 2 mm projectiles. Linear and power law fits are shown to the combined data sets in each case (see Eqs. (1)–(4) in the main text).

and,

$$S = (103,100 \pm 59,686)P^{-(2.08 \pm 0.25)}, \quad (1 \text{ mm}), \quad r = -0.9855 \quad (7)$$

$$S = (541,175 \pm 556,750)P^{-(2.44 \pm 0.42)}, \quad (2 \text{ mm}), \quad r = -0.9792 \quad (8)$$

where r is the regression coefficient of the fit (a negative value in this case due to an inverse correlation), S is in μm , v in km s^{-1} and P in GPa. Whilst the overall scale coefficient differs between the 1 and 2 mm data sets, in each case the powers agree within 1σ .

Given that the mean fragment size seems to follow a similar power law behaviour, we normalise the mean fragment size by the original projectile size and re-plot the data in Fig. 5. We again fit the data, but this time we make a combined fit to both the 1 and 2 mm data sets. As before, we excluded the data from the shots below 2 km s^{-1} (they did not fragment) and attempted both linear and power law fits. We find:

$$SN = (1.24 \pm 0.21) - (0.218 \pm 0.048)v, \quad r = -0.8017 \quad (9)$$

$$SN = (23.5 \pm 7.1)v^{-(3.50 \pm 0.31)}, \quad r = -0.9804 \quad (10)$$

and,

$$SN = (0.855 \pm 0.148) - (0.021 \pm 0.006)P, \quad r = -0.7471 \quad (11)$$

$$SN = (107 \pm 47)P^{-(2.08 \pm 0.18)}, \quad r = -0.9801 \quad (12)$$

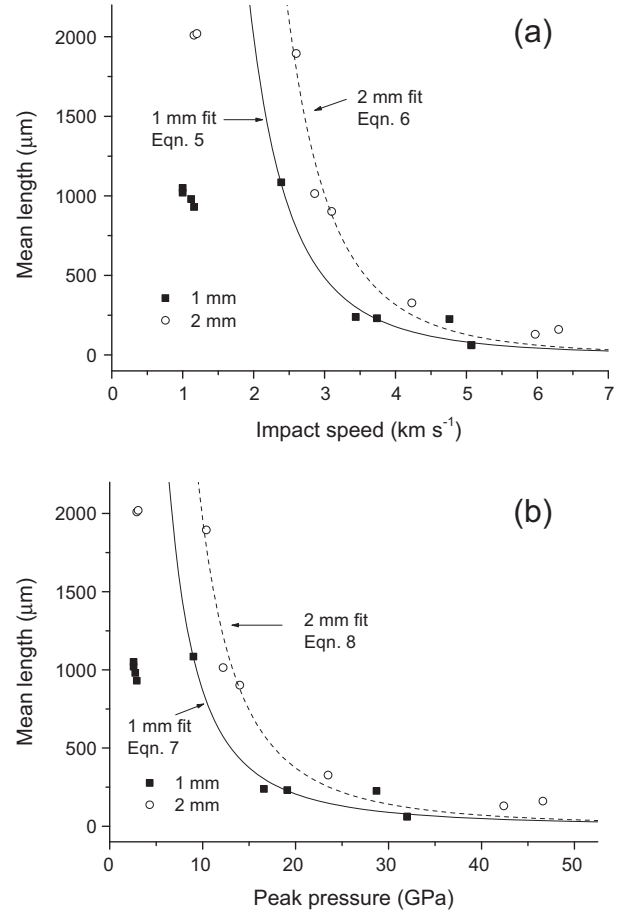


Fig. 4. The mean length of the projectile fragments vs. (a) impact speed and (b) peak pressure corresponding to each speed. Black squares represent 1 mm projectiles, circles represent 2 mm projectiles. A power law fit is shown for each data set separately (see Eqs. (5)–(8) in the main text).

where SN is the normalised fragment size, r is the regression coefficient of the fit, v is in km s^{-1} and P in GPa. As suggested by the regression coefficients, the power law fits provide a better description of the data, and, indeed, the linear fit suggests that at around 5.7 km s^{-1} there should have been no fragments, in disagreement with the data. These results imply that a given peak pressure causes the same degree of fragmentation on this size scale. If we extrapolate the power law fit results to a normalised fragment size of 1, this implies that significant deformation occurs once an impact speed of 2.4 km s^{-1} (peak shock pressure of 7 GPa) is obtained. The impact speed to actually fragment the projectiles was found experimentally to be below 2.4 km s^{-1} (and 7 GPa), just around the predicted values.

The collected mass of the projectile fragments normalised by the original mass is shown vs. impact speed and peak pressure in Fig. 6a and b respectively. A negative correlation is observed implying that during fragmentation some of the projectile material is lost. We fit the recovered mass fraction with both linear and power law functions (note that, as usual, the impacts at less than 2 km s^{-1} were not included in the fits as they had not fragmented). We found:

$$M = (1.03 \pm 0.21) - (0.147 \pm 0.049)v, \quad r = -0.7485 \quad (13)$$

$$M = (3.02 \pm 1.97)v^{-(1.54 \pm 0.60)}, \quad r = -0.7734 \quad (14)$$

and,

$$M = (0.782 \pm 0.140) - (0.0149 \pm 0.005)P, \quad r = -0.7300 \quad (15)$$

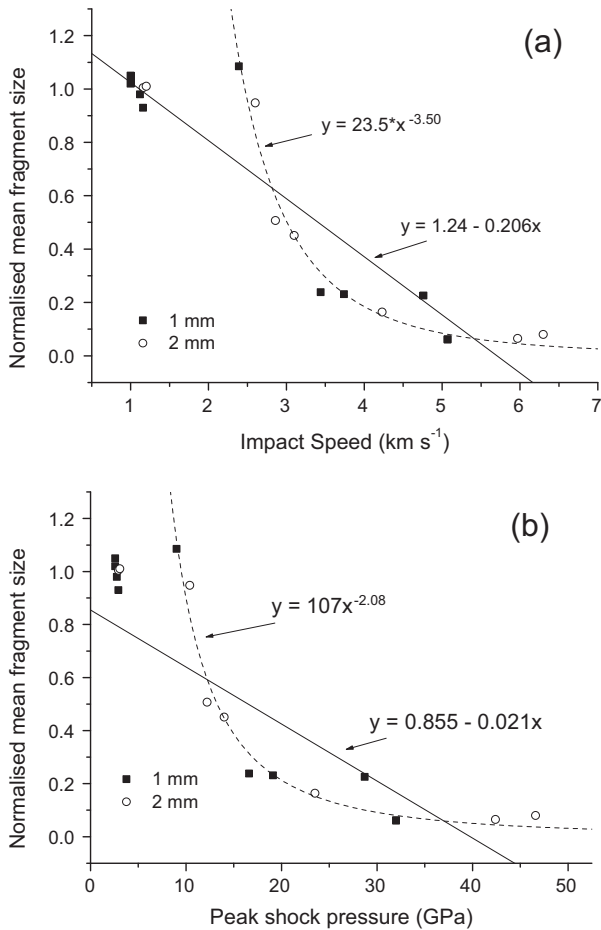


Fig. 5. The length of the projectile fragments normalised to original projectile diameter vs. (a) impact speed and (b) peak pressure corresponding to each speed. Black squares represent 1 mm projectiles, circles represent 2 mm projectiles. Linear and power law fits are shown to the combined data sets in each case (see Eqs. (9)–(12) in the main text).

$$M = (5.88 \pm 5.36)P^{-(0.917 \pm 0.357)}, \quad r = -0.7733 \quad (16)$$

where M is the recovered mass fraction, r is the regression coefficient of the fit, v is in km s^{-1} and P in GPa. There is very little difference in quality of the fits between the linear and power law hypotheses, but we note that the linear fit suggests no mass would be recovered above an impact speed of 6.99 km s^{-1} , whereas the power law fit does extrapolate to higher speeds.

In Fig. 6 it is clear that we immediately see a significant mass loss as soon as fragmentation occurs, i.e., 2.39 km s^{-1} (9.1 GPa). It is possible that, once fragmented, some projectile material may be lost through (i) production of increasing numbers of small fragments below our detection limit, (ii) increasingly amounts of projectile material may be lost through mixing with the impact ejecta, or (iii) the on-set of vaporisation at higher speeds.

The Cu projectiles that experienced peak pressures around 9 GPa begin to show evidence of fragmentation and lost mass. Shot number G051202 (1 mm at 2.39 km s^{-1} , peak pressure of 9.1 GPa) is the first 1 mm projectile shot to show fragmentation, with the projectile breaking into one large and one smaller fragment (Fig. 7), the larger of which had a maximum linear dimension greater than the diameter of the original projectile. This shows that at this impact speed, the peak shock pressure produced during the impact is not sufficient enough to cause catastrophic breakup of the Cu projectile (defined as the largest surviving fragment having less than 50% of the original projectile mass), but rather that the

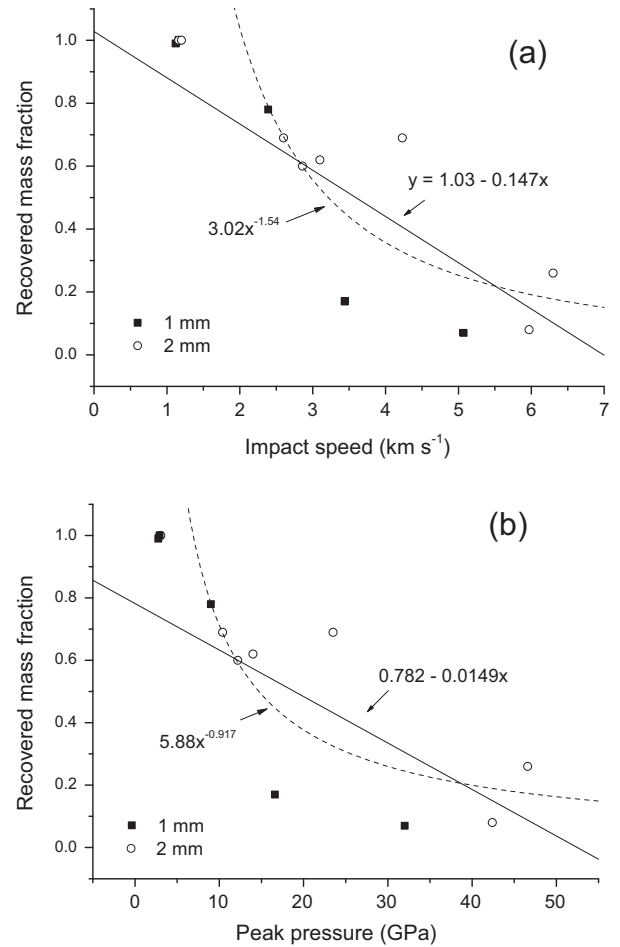


Fig. 6. Recovered projectile mass fraction vs. (a) impact speed and (b) peak pressure corresponding to each speed. Black squares represent 1 mm projectiles, circles represent 2 mm projectiles. Fits are shown to the combined data sets in each case (see Eqs. (13)–(16) in the main text).

projectile experiences sufficient stress to cause a significant strain deformation resulting in the elongated shape of the fragments. The fragmentation of the projectile at these peak pressures is more likely a result of ductile deformation rather than catastrophic failure of the whole projectile as is observed with the projectiles which experienced greater peak pressure. This type of fracture is different to that observed in brittle projectiles, where the on-set of fragmentation is usually via a meridian splitting effect which produces two near hemi-spherical fragments (e.g., see Burchell et al., 2009, for a discussion).

One shot at 7.05 km s^{-1} (estimated peak shock pressure of 56.7 GPa) caused such extreme fragmentation of the copper projectile that from filtration and extraction alone, no copper material could be collected for analysis in the SEM. Instead, the projectile material was observed as micron sized particles which were entwined within the fibres of the filter paper. Even allowing for the large number of observed fragments trapped in the filter paper, their small size means they do not represent a significant mass. Thus the small volume and mean size of the projectile fragments at high peak pressures ($>56.7 \text{ GPa}$) suggests that the majority of the projectile mass is lost with the uncollected ejecta and/or was vaporised, although many small, fine fragments may remain in the target.

The cumulative fragment size distributions are shown in Fig. 8. We show the data for the 1 mm and 2 mm projectile sizes separately (both normalised to initial projectile size). In both, cases

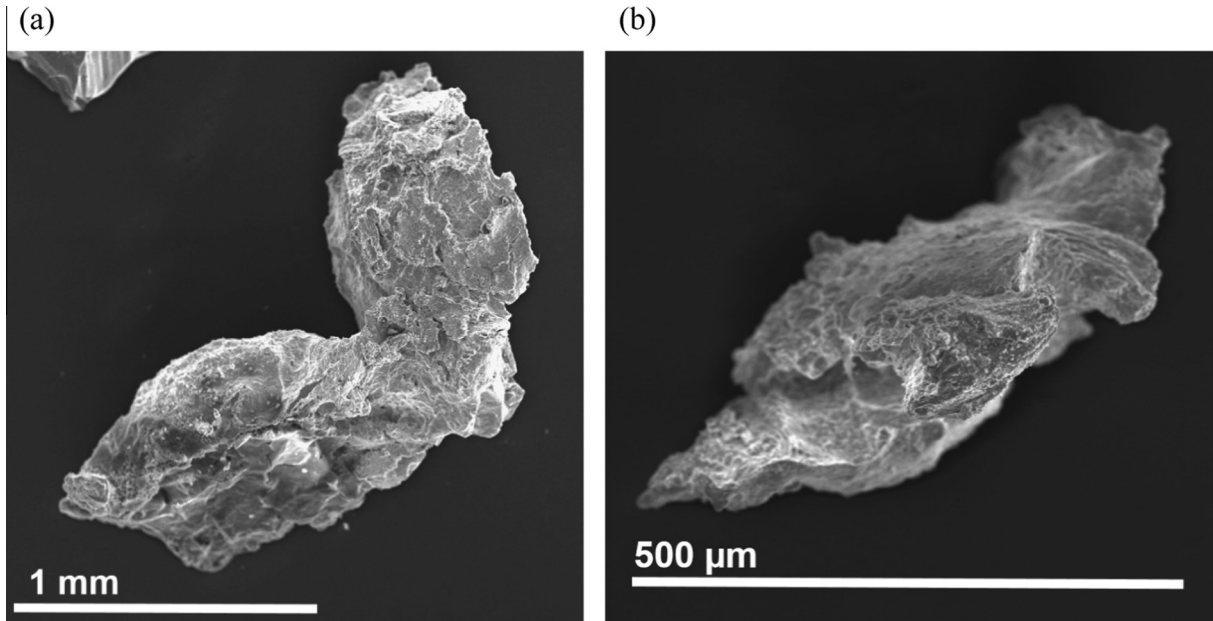


Fig. 7. Secondary electron images (20 kV) of the two fragments from shot G051202#1 produced after an impact of a 1 mm projectile at 2.39 km s^{-1} , showing (a) the elongation of the largest fragment and (b) the smaller detached fragment.

the data fall into two main distributions. At low speeds ($2\text{--}5 \text{ km s}^{-1}$) the largest (normalised) fragment size is still relatively large, so the data start at the right hand side of the plots. Note that it is possible for a fragment to exceed the original projectile size if it has been elongated during the impact and thus the normalised size can exceed 1.0. In effect we only measure size in two dimensions (length and width) and in such a case the depth will be reduced to conserve overall mass. As the speed increases from 2 to 5 km s^{-1} the largest fragment size slowly decreases in size. However, at around 5 km s^{-1} there is a sudden larger decrease in the size of the largest fragment, moving the cumulative size distributions leftward on the plots in Fig. 8. The slope of the cumulative size distributions also increases.

When grouped by impact speed, some of the cumulative size distributions in Fig. 8 diverge at certain sizes. For example, in Fig. 8a, the data set for the 3.44 km s^{-1} impact diverges from those for 3.74 and 4.76 km s^{-1} at a (normalised) size of around 0.4. However, below a size of 0.2 the slopes in the data at all three speeds appear similar (see below for numerical details of the slopes). This suggests that a few fragments were not recovered in some of the data sets at around a size of 0.2–0.4. Given that this size is quite large and hard to miss in our extraction or analysis, the most likely explanation for their loss is that they were carried away from the crater by ejecta. That projectile material can be carried away from the impact site on target ejecta is reported in experiments elsewhere (e.g., see Burchell et al., 2012).

In order to quantify the slope of the cumulative (normalised) fragment size distributions we use the more complete distributions in each of Fig. 8a and b, selecting one in the low speed ($<5 \text{ km s}^{-1}$) and one in the high speed ($>5 \text{ km s}^{-1}$) region in each case. The selected data are shown in Fig. 9 and the data were then fitted. In each case the smallest and largest sized data were excluded from the fits. This avoids bias from decreasing collection efficiency at small sizes, and at the largest sizes avoids the step change in the largest fragment sizes visible in some of the data. The fit results for the 1 mm data in Fig. 9a, are:

Low speed (3.44 km s^{-1})

$$N = (0.76 \pm 0.10)d^{-(1.67 \pm 0.07)}, \quad r = -0.9473 \quad (17)$$

At high speed (5.07 km s^{-1}) we had to make separate fits at small and large sizes, giving,

$$N = (0.0017 \pm 0.0003)d^{-(3.20 \pm 0.06)}, \quad r = -0.9942, \quad \text{for } d < 0.075 \quad (18)$$

and

$$N = (0.0043 \pm 0.0043)d^{-(3.12 \pm 0.45)}, \quad r = -0.9694, \quad \text{for } d > 0.09 \quad (19)$$

Given the similarity in slope at small and large sizes in the fit to the high speed data, we suggest this is a continuous distribution, but that one or two fragments were lost (either from the crater itself as ejecta or during the analysis) at around a normalised size of 0.08, causing a kink in the distribution.

The 2 mm data (Fig. 9b) were also fit and gave:

Low speed (4.23 km s^{-1})

$$N = (2.27 \pm 0.13)d^{-(1.79 \pm 0.03)}, \quad r = -0.9900, \quad \text{for } d < 0.25 \quad (20)$$

and

$$N = (0.38 \pm 0.04)d^{-(3.04 \pm 0.08)}, \quad r = -0.9950, \quad \text{for } d > 0.25 \quad (21)$$

Two fits were required at low speed as the slope changed distinctly at smaller and larger sizes.

High speed (5.97 km s^{-1})

$$N = (0.069 \pm 0.004)d^{-(2.70 \pm 0.02)}, \quad r = -0.9967 \quad (22)$$

Looking at the fit results, it appears a slope of around -1.7 characterises the data at low speed, whereas a slope of -3 is more typical at high speeds. The exception is the 2 mm diameter projectile impact at 4.23 km s^{-1} . Here the larger fragments obey a slope of -3.0 , whereas the smaller fragments still follow a slope of -1.79 . We suggest that this impact is approaching the threshold speed to more complete projectile disruption, and the data set is therefore showing a transition from the more shallow to the steeper slope, and that this is showing up first in the relatively larger fragments.

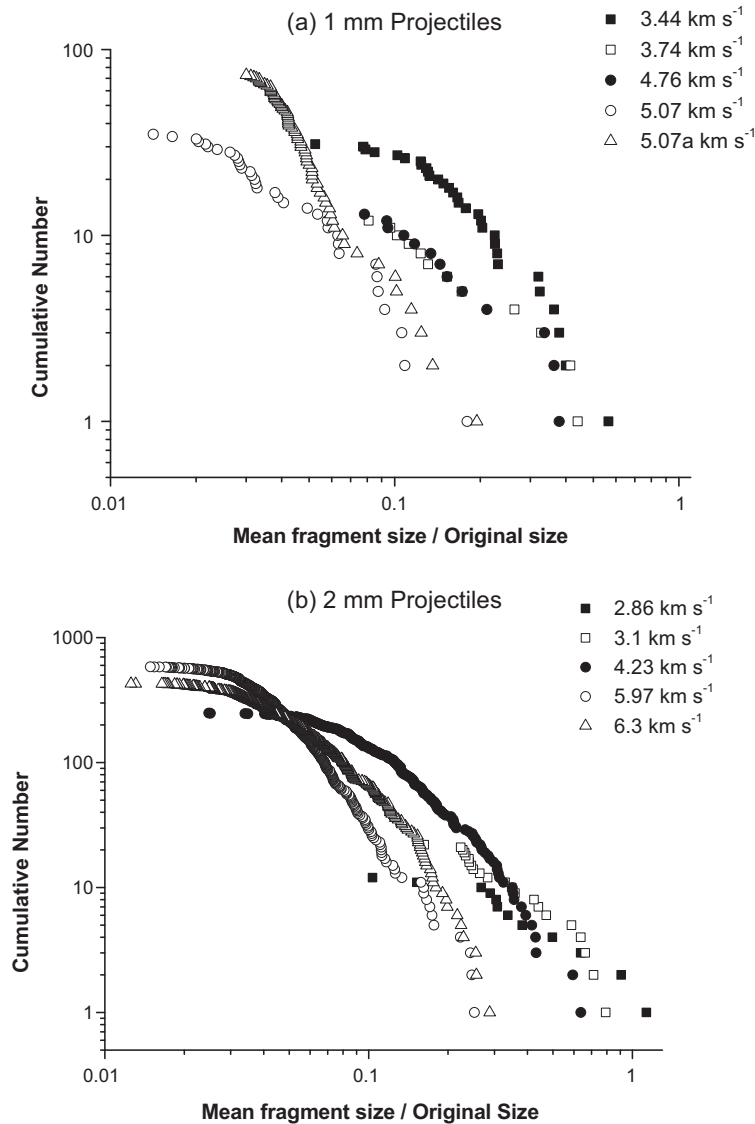


Fig. 8. Cumulative size distributions for recovered projectile fragments where fragment size has been normalised to original projectile diameter. (a) 1 mm projectiles and (b) 2 mm projectiles. In both (a) and (b) the data follows two trends, with the data grouped similarly in the speed range 2–5 km s⁻¹ at the right hand of each plot, but moves to the left of the plot for speeds above 5 km s⁻¹. See text for a fuller discussion.

4. Discussion

From the data produced by this analysis we identified four possible stages of the disruption and fragmentation of the Cu projectile (see Table 3) with the degree of projectile deformation linked to the impact speed and thus peak shock pressures experienced. To aid the following discussion, examples of the recovered projectile material are shown in Figs. 1, 2 and 7, and in Figs. A1 and A2 in Appendix A. The first stage occurs at speeds between 1.0 km s⁻¹ (2.3 GPa) and approximately 2.0 km s⁻¹ (6.8 GPa). The projectile experiences only slight alteration with the surface of the spheres becoming pitted and cracked on the surface with some evidence of bulk deformation appearing (see shot G081002#2 in Fig. A2). The second stage occurs at shot speeds between 2.0 (6.8 GPa) and 2.39 km s⁻¹ (9 GPa) where both the 1 mm and 2 mm projectiles experience ductile deformation resulting in elongation of the projectile and, in one case, at the higher end of this speed regime, shearing and separation of the projectile into two parts. The third stage occurs for shot speeds of 2.6 km s⁻¹ (10.4 GPa) and beyond. Here both the 1 mm and 2 mm projectiles break up

into multiple fragments as a result of catastrophic deformation of the projectile. For speeds above 2.6 km s⁻¹ (10.4 GPa) the number of fragments produced increases significantly, with fragment numbers exceeding 500, with impact speeds of around 6 km s⁻¹. At the same time, the mean size of the fragments decreases. We also identify a fourth stage (>5 km s⁻¹, >32 GPa). Above this speed the largest fragment suddenly decreases in size, the slope of the cumulative number of fragments vs. size increases from -1.7 to around -3, the mean fragment size falls below 10% of the initial projectile size and the rate of increase in fragment numbers slows (as does the rate of decrease in mean fragment size). The speed of 5 km s⁻¹ thus represents the transition from partial to complete disruption of the projectile.

Loss of material mass is observed in the projectiles in experiments using shots speeds greater than 2.0 km s⁻¹ in both the ductile deformation and fragmentation stages of deformation of the projectile. At speeds greater than 2.6 km s⁻¹, where the projectile experienced catastrophic disruption, the loss in material maybe the result of partial vaporisation of the projectile at the point of impact, and/or loss of projectile material that may have been

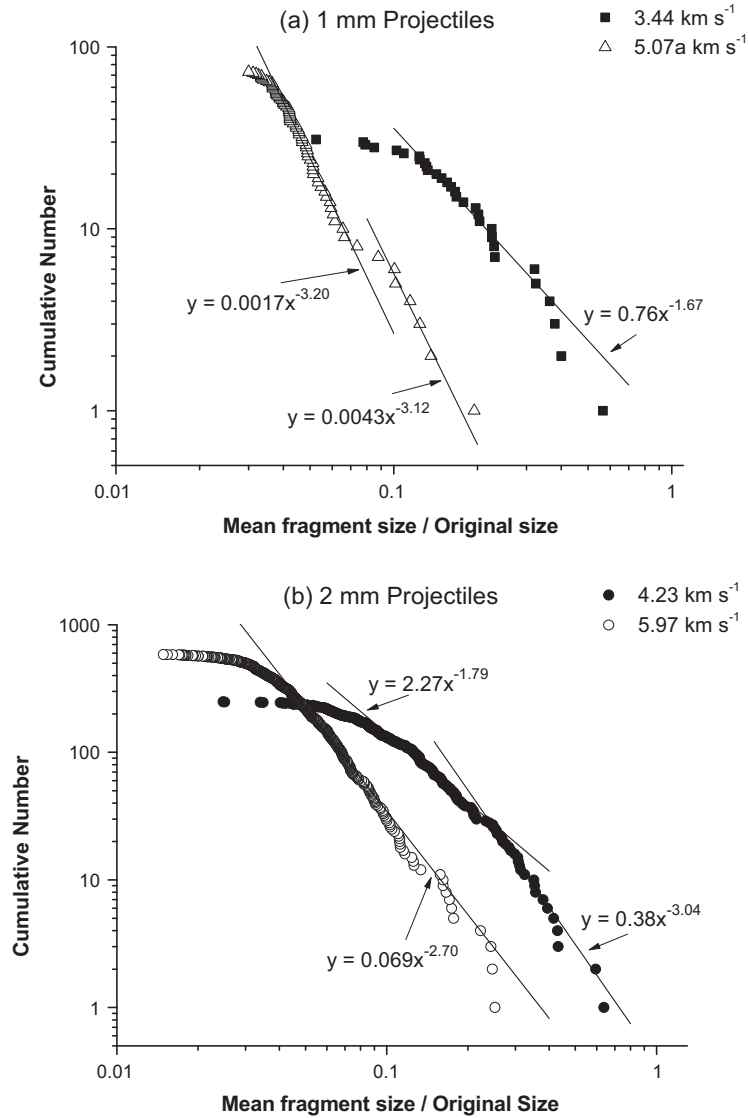


Fig. 9. Fits to cumulative size distributions for recovered projectile fragments where fragment size has been normalised to original projectile diameter. (a) 1 mm projectiles and (b) 2 mm projectiles. In both (a) and (b) two impacts are shown, one at an impact speed less than 5 km s⁻¹ and one at higher speed. The fits shown are power law fits described in the text (see Eqs. (17)–(22) in the main text).

Table 3
Summary of projectile fate.

Stage	Description	Impact speed (km s ⁻¹)	Peak pressure (GPa)
I	Little effect, some surface pitting and minor deformation	1.0–2.0	2.5–6.8
II	Increasing ductile deformation, onset of breakup	2.0–2.5	6.8–9.0
III	Increasing fragmentation	>2.6	>10.4
IV	Complete disintegration and substantial mass loss	>5.0	>32.0

ejected away from the target body during the impact. One possibility is that not all the material is collected during the analysis. However each shot was collected using the same methodology and equipment described above, meaning that any bias from this method is negated when comparing the size and mass distribution of the whole data set. This still permits systematic loss, but the small size of the fine fragments which are not separable from the

filter paper means that they contain relatively little mass. The slight loss in mass observed in the projectile material that experienced ductile deformation is more difficult to explain. For ductile deformation and strain to occur it is likely that the shock experienced was not sufficient to cause vaporisation. One possibility is that the pitting and cracking on the surface of the projectile has resulted in material being lost from the surface during the ductile deformation, this may have been too fine to collect with our method or, have then been carried away with the ejecta during crater formation.

Both the 1 mm and 2 mm projectile sizes experience a sudden reduction in the mean fragment size at about 2.8 km s⁻¹ (11.8 GPa) – see Fig. 5a. This may indicate that around this velocity the peak shock pressure produced exceeds the ultimate yield strength of the Cu projectiles and results in catastrophic fragmentation of the projectile. Once this limit has been exceeded then increasing the shot speed, and hence peak shock pressure, results in a greater degree of fragmentation and disruption to the projectile until the energy released during unloading of the projectile causes the projectile to vaporise. Interestingly the number of

fragments produced and the recovered normalised mass do not show the same sudden jump with increasing shot speed shown in Table 3; instead both variables have a shallower dependence on shot speed.

4.1. Comparison to other laboratory experiments

A study of fragmentation of aluminium spheres during hypervelocity impacts onto Al sheets, reported by Piekutowski (1995), shows the same deformation stages as observed here, beginning with (1) plastic (ductile) deformation of the impacting surface, (2) the formation of a spall failure at its rear surface, (3) development of a detached shell of spall fragments, and (4) complete disintegration of the sphere. Note that Piekutowski (1995) only labelled three stages, which are here called stages 2–4, neglecting to label the plastic deformation regime as the first stage and thus treating it, in effect, as a preliminary stage 0. Here we number the regimes from 1 to 4, with plastic deformation as stage 1, as this means that each physical regime is now labelled. Piekutowski, used a projectile diameter of 9.53 mm, which, having penetrated (thin) Al target plates, produced fragments which were imaged in flight by radiographs, allowing a detailed study of the breakup of the projectile arising from the impact. As with the observation from this study, Piekutowski (1995) found that as impact velocities increased severe deformation of the projectile occurred, and that the threshold impact velocity for failure inside the rear surface of the sphere changed with the ratio of target thickness/projectile diameter. The work reported here used much smaller projectiles impacting against an effectively semi-infinite target so should be taken as having an endpoint (maximal) value of the ratio target thickness/projectile diameter, however the general evolution of the breakup identified by Piekutowski (1995) is also observed in the (smaller scale) experiments reported here. There is one difference however, in that the second stage was not fully observed for the impacts here. This could partly be due to the measurements here being made subsequent to the impact, with no knowledge retained as to the leading and trailing faces of the spherical projectile at the moment of impact. In Piekutowski (1995) the on-set of projectile failure (i.e., the start of stage 3) occurred at a constant impact speed around 2.6 km s^{-1} in impacts on thick targets which were defined as having a thickness more than 16% of the projectile diameter. Here, with a different projectile material (copper vs. aluminium) and an effectively semi-infinite target, we still find a very similar impact speed threshold.

Projectile deformation during impacts on sand (a porous target) at speeds from 0.5 to 2.8 km s^{-1} is discussed in Schultz and Gault (1984). Over this speed range, they reported that aluminium projectiles start to deform at 0.5 km s^{-1} , have essentially flattened at 1 km s^{-1} , the flat sheet bends into a cup shape at 2 km s^{-1} and fragmentation occurs at 2.8 km s^{-1} . They noted that the shock pressures generated in the impact exceeded the (aluminium) projectile compressive strength at between 1.5 and 2 km s^{-1} .

Other, more recent, work (Kenkmann et al., 2013) investigated 10–12 mm diameter steel sphere projectile deformation during hypervelocity impacts at 2.5 – 5.3 km s^{-1} into wet and dry sandstone blocks. They reported no significant trend between impact energy, the presence of water in the target and the mass of the projectile recovered after impact. However, projectile fragmentation appeared to increase if the target contained substantial amounts of water, suggesting that the shock history played an important role in the fragmentation. In impacts on dry sandstone at speeds up to 5.34 km s^{-1} , Kenkmann et al. (2013) typically recovered over 70% of the impactor mass from the crater, usually in a single large bowl-shaped fragment. However, if the sandstone contained water (with thus a different shock history during the impact) multiple fragments were obtained, and in one case at 5.7 km s^{-1} , the frag-

ments were described as “tiny”, each being less than 10% of the original projectile diameter. Kenkmann et al. (2013) used the PIA to predict peak shock pressures in their dry sandstone targets as being in the range 40–70 GPa, similar to those here, but do not estimate shock pressures in the wet sandstone targets. Comparing the mean fragment size here in the range 40–70 GPa (see Fig. 5b) with that of Kenkmann et al. (2013) we observe that both report sizes of order 10% of the original length.

We also compare the results here with those of Hernandez et al. (2006), who fired stainless steel projectiles at various metal targets. They observed the on-set of projectile disruption at about 0.7 km s^{-1} , which they estimated to a peak shock pressure of around 14 GPa. Fragment size then decreased until, at their highest speed (5.2 km s^{-1} , estimated peak shock pressure of 174 GPa), the average fragment size was of order 10% of the original diameter. Hernandez et al. (2006), made a linear extrapolation of their results to suggest no fragments would survive at 6 km s^{-1} , but the hydrocode simulations they performed suggested that projectile fragments should still be present in their craters at 10 km s^{-1} . The peak shock pressure values found by Hernandez et al. (2006) for the onset of fragmentation and mean fragment size of 10% of the original diameter, are higher than those found here, but apply to stainless steel rather than copper. We note that at strain rates up to 10^4 s^{-1} , the yield strength of copper is around 300 MPa (see Price et al., 2013 for a discussion), whereas for stainless steel 316L (a typical steel) the yield strength is $\sim 1 \text{ GPa}$ (Lee et al., 2011). At higher strain rates these yield strengths rise significantly. So the nature of the projectile material can play a role in determining the impact speed and shock pressure thresholds for fragmentation.

4.2. Relevance to planetary science

4.2.1. Deep Impact

The impactor from the *Deep Impact* mission collided with Comet Tempel-1 at speeds which are beyond those reported here. The speed of the *Deep Impact* collision was recorded at being 10.3 km s^{-1} (Veveřka et al., 2013), which we estimate would have produced a PIA peak shock pressure of 111 GPa, assuming a solid copper body hitting a solid water ice body. However, this needs to be adjusted for both impact angle and target porosity. Following the approach of Pierazzo and Melosh (2000), we adjust the peak shock pressure by $\sin \theta$ (where θ is the impact angle), lowering the estimated peak pressure to 55 GPa. The influence of porosity is harder to estimate as it is present in both target and projectile to differing degrees. For example, estimates suggest the surface of Tempel-1 was approximately 90% porous (see Schultz et al., 2007 for a discussion). This however is likely to consist of a range of void space sizes. In the impactor, the overall bulk density was low, not only due to the volume of the overall craft but also due to a leading copper mass with large void spaces milled out of stacked copper slabs in the form of a hemisphere. From the literature we can consider general behaviour due to porosity. For example, if two similar sized bodies collide at 5 km s^{-1} , Davison et al. (2010) estimate that peak shock pressure can fall by 75% if both bodies are 50% porous. However, a separate hydrocode study (Potter and Collins, 2013) suggests that in impacts of a dunite projectile on a non-porous target at 12 km s^{-1} , the fraction of the impactor that survives falls from 40% to 10% as projectile porosity is increased from 0% to 10%. Potter and Collins therefore suggest that to maximise projectile survival in an impact, its porosity must be minimal. A detailed hydrocode simulation of this (including the influence of porosity and compaction of pore spaces) is thus required but is not currently available.

We therefore take two approaches to explore how the copper mass may have fragmented in the *Deep Impact* event. First, scenario

1, we simply extrapolate our experimental data (taken for normal incidence impact of a non-porous copper mass into ice with 50% porosity) to the *Deep Impact* speed of 10.3 km s^{-1} . This assumes zero porosity in the impactor, and does not allow for the 30° impact angle. The second approach, scenario 2, is to predict behaviour at a peak shock pressure of 55 GPa (estimated from the PIA at 10.3 km s^{-1} adjusted for the non-normal incidence impact). This shock pressure is similar to that estimated in our hydrocode modelling for a normal incidence impact at just above 7 km s^{-1} . Again, the role of projectile porosity is not allowed for. These two scenarios are thus indicative of the range of possible impact outcomes based on impact speed and angle of incidence, but do not account for the detailed porosity in the projectile.

Scenario 1: The highest shot speed achieved as part of this study was 7.05 km s^{-1} (56.7 GPa). At this speed little to no separable material was collected during the filtration method. Instead the copper material that was collected was micron sized, rounded fragments which could not be handled or weighed with our existing analysis methods. Therefore, even at this speed, not all the material is vaporised or lost from the target with the ejecta, meaning that at similar impact speeds projectile material may possibly exist underneath and within craters which form on comets and similar porous ice bodies. Extrapolating the results here vs. impact speed (in Fig. 3a) to 10.3 km s^{-1} , we predict that for a linear fit (Eq. (1)) there would be 803 fragments beneath the crater, whilst from the power law fit (Eq. (2)) we estimate 9778 fragments. Taking these different extrapolations as indicating the uncertainty in the results, we thus estimate that between one to ten thousand fragments will be present beneath the crater. Given that the power law behaviour was a better description of the data in Fig. 3a the number of fragments is likely to be at the higher end of this estimate. The mean fragment size can also be predicted. Based on the results in Fig. 5a, we use the power law fit (Eq. (10)) to predict that the mean fragment size (at an impact speed 10.3 km s^{-1}) will be 0.7% of the original impactor size, i.e., given a 1 m diameter copper impactor the mean fragment size will be 7 mm. The recovered mass fraction (Fig. 6a) was fit with a power law fit (Eq. (14)), and extrapolating this to an impact speed of 10.3 km s^{-1} , suggests that some 8% of the impacting mass would be recoverable.

Scenario 2: requires similar estimates to be made at a given peak shock pressure, here estimated as 55 GPa. As stated, this is very close to the peak pressure regime obtained in our experiments, so the extrapolation is likely to be more reliable. The number of fragments expected at 55 GPa is 495 (linear fit, Eq. (3)) or 925 (power law fit, Eq. (4)). The mean fragment size is 2.6% of the original size (power law fit, Eq. (12)), i.e., a 1 m diameter copper mass would yield fragments with a mean size of 26 mm. Lastly, the recoverable mass fraction is estimated at 15% (power law fit, Eq. (16)).

Taken together, these scenarios suggest that the number of copper fragments likely ranges from ~ 500 to 10,000, with mean size estimated to lie between 7 and 26 mm, and with some 8–15% of the original copper mass recoverable at the crater site. The influence of the structure and porosity of the projectile still needs to be included; so, these should be taken as estimates rather than detailed predictions. In terms of surviving projectile mass, it should also be considered that some material will have been carried away from the crater as impact ejecta (e.g., see Schultz and Gault, 1990, who showed projectile fragmentation with material carried away from the target in shallow angle impacts, and also see Burchell et al., 2012, who showed experimentally that even in normal incidence impacts projectile material can be carried away from an impact site and collected in secondary impacts on witness materials). Thus more copper material may have survived the impact but not be present at the impact site. It should be noted however that this assumes a pure water ice target. In reality, a comet will also have a rocky component mixed in with the ice.

4.2.2. LCROSS

It is also possible to consider what happened in the LCROSS impact on the Moon in 2009 when a spent Centaur rocket upper stage and a separate shepherding spacecraft, were deliberately directed into impacts with the lunar surface. The intention was to look for volatile (ice) rich material in these regions. The Centaur impact occurred at 2.5 km s^{-1} in a permanently shadowed region in Cabeus crater near the lunar south pole. The resulting crater from the impact was estimated to be 25–30 m diameter (Schultz et al., 2010). A later review confirmed the impact speed as being 2.5 km s^{-1} . The impact was always planned to be at a high angle to the local surface and the impact was subsequently measured to be (3.7 ± 2.3) from normal incidence on the surface (Marshall et al., 2012). A separate study (Hermalyn et al., 2012) also suggested an impact at 85° from the local horizontal, i.e., near vertical. Given the relatively low impact speed, the data here suggest a small number of fragments of considerable size should be retained at the impact site. However, the LCROSS impactor was not a single distinct, compact mass, but was a Centaur upper stage, with a mass concentrations such as the steel fuel tank and the engine, at one end. The whole body however had much empty space and thus an effective overall density of 25–30 kg m^{-3} (see Hermalyn et al., 2012 for a fuller description). There will have been concentrations of mass inside the stage, but these will have impacted the surface in sequence. The role of the large void spaces in the projectile in determining the outcome of the impact was discussed in Schultz et al. (2010). Subsequently, Hermalyn et al. (2012) reported impact experiments using hollow projectiles which reflect the behaviour of the main Centaur components (e.g., the fuel tank). They found that the hollow nature of the impactors alters for example the depth of penetration (which is reduced), the depth from which ejecta is excavated (also reduced) and produces a more complicated sequence of angles of ejection. They also predict survival at the impact site of crushed fragments of the Centaur rocket. Another way of considering this type of impact is as if by a segmented impactor, a method known to change the results of an impact (see the recent discussion by Ben-Dor et al., 2010 and references therein). However, segmented impactors tend to have regularly spaced similar masses unlike here, so caution should be taken with applying such an approach to allow for the non-uniform nature of the mass distribution in the Centaur. Clearly however, this distribution of mass inside the impactor significantly complicates predictions of survival of impactor material. The impact speed itself places this event at the top end of Stage II defined in Table 3. The major masses in the Centaur rocket are not likely to have broken up to a significant degree due to the relatively low impact speed. However, the thin side panels of the rocket may well have broken into many pieces during the impact, as indeed would any of the material initially in thin sheet form rather than a compact mass. Indeed, as noted by Hermalyn et al. (2012), there is likely to be a significant fraction of the rocket retained at the impact site in a highly crushed form.

4.2.3. Meteorites on the martian surface

As well as man-made impacts we can also consider the case of impacts on the martian surface. When considering the survival of material arriving at Mars, Bland and Smith (2000) considered that the main source of non-indigenous material on the martian surface was from small meteorites decelerated during passage through the atmosphere to a speed of less than 1 or 2 km s^{-1} (and which thus survive the impact relatively intact). The only other source they could envisage was for stress-wave interference to reduce the shock on a small portion of an impactor (at the rear of the body). However, they did not expect this to produce significant survival of projectile material in a high speed impact. More recent analyses based on observed iron meteorites on Mars (e.g., that of Fairen

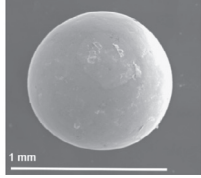
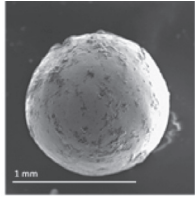
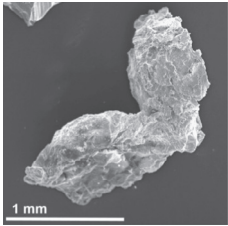
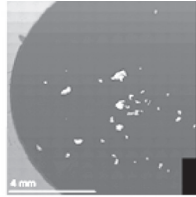
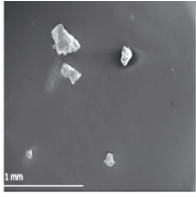
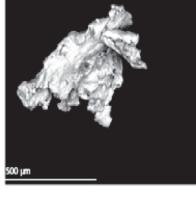
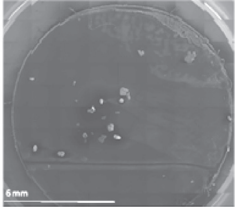
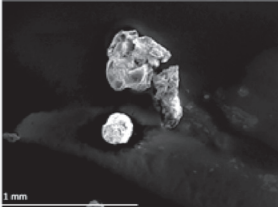
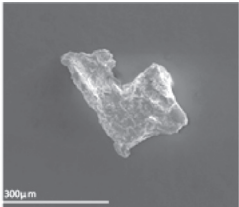
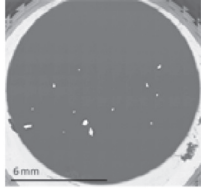
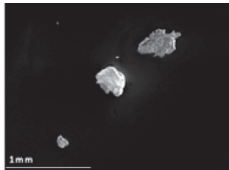
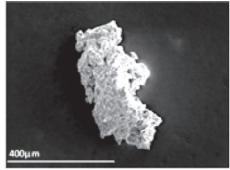
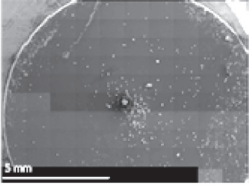
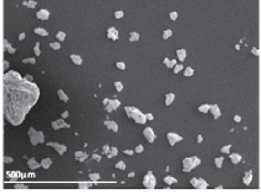
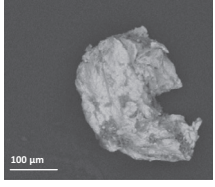
Shot No.	Low Resolution	Intermediate resolution	High Resolution
Pre-shot			
G30702#1 1.12 km s ⁻¹			
G051202#1 2.39 km s ⁻¹			
G291104#1 3.44 km s ⁻¹			
G291104#3 3.74 km s ⁻¹			
G111202#1 4.76 km s ⁻¹			
G240205#3 5.07 km s ⁻¹			

Fig. A1. Secondary electron images of copper fragments from impacts of 1 mm diameter projectiles onto porous ice. The varied shapes become apparent in the intermediate resolution images where many fragments can be seen at once. The nature of the fine detail on individual fragments can be seen in the high resolution images of individual fragments.

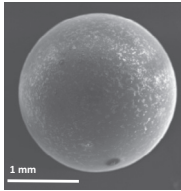
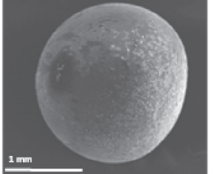
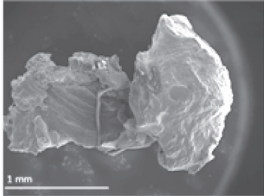
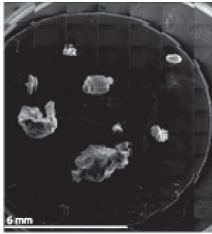
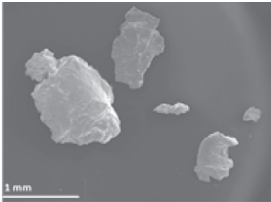
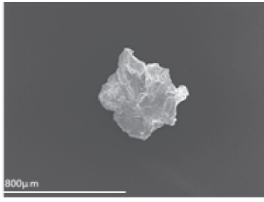
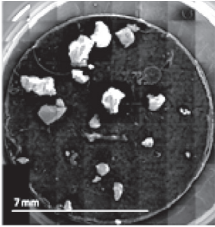
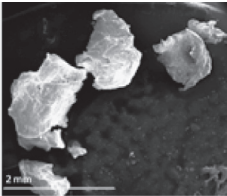
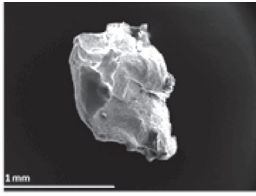
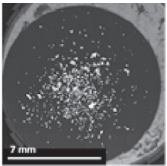
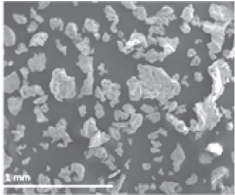
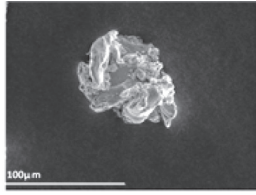
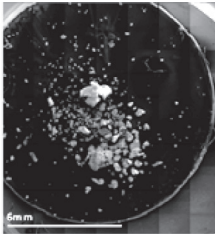
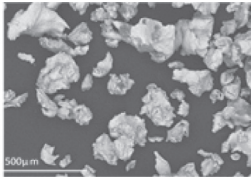
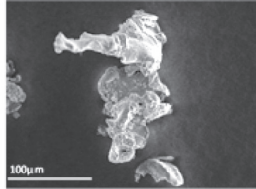
Shot No.	Low Resolution	Intermediate resolution	High Resolution
Pre-shot			
G081002#2 1.2 km s ⁻¹			
G250603#1 2.6 km s ⁻¹			
G300902#1 2.86 km s ⁻¹			
G011002#1 3.1 km s ⁻¹			
G121002#2 5.97 km s ⁻¹			
G270603#1 6.3 km s ⁻¹			

Fig. A2. Secondary electron images of copper fragments from impacts of 2 mm diameter projectiles onto porous ice. The varied shapes become apparent in the intermediate resolution images where many fragments can be seen at once. The nature of the fine detail on individual fragments can be seen in the high resolution images of individual fragments.

et al., 2011 looking at six iron meteorites of sizes 30–60 cm reported by the Mars Exploration Rover Opportunity in a 25 km traverse across Meridani Planum), reach similar conclusions. That is they favoured the origin of the meteorites observed on the surface as being from the falls of small bodies which decelerated in a dense atmosphere. In this case, Fairen et al. (2011) based their findings on observation of the surfaces of the particular bodies observed on the martian surface, consideration of their likely age (over 3 Gya), the setting in which they are found and so on. The survival of so many individual iron meteorites in a limited region could be caused by coincidence or accumulation over time.

However, if we consider the general case of the arrival of a larger metallic body, say in excess of 1 m across, then its impact speed on the surface in the modern era of a low density atmosphere, will not have been significantly reduced. Various estimates exist for the distribution of speeds for bodies arriving at Mars. The speed distributions typically range from 5 km s^{-1} (the martian in-fall speed) and peak at around 10 km s^{-1} (e.g., 10.2 km s^{-1} , see Flynn and McKay, 1990). This peak speed is usually taken as typical and is similar to the *Deep Impact* case considered above. However, Le Feuvre and Wieczorek (2011) suggest a lower mean speed as they predict a second peak in the distribution of speed at just above 5 km s^{-1} . This suggests a high probability of an impact speed in the range $5\text{--}10 \text{ km s}^{-1}$, similar to that considered in this paper. Such an impact could indeed occur in a polar or ice rich region making the current experiments even more relevant. Based on the results above, we thus suggest that between 25% and 8% of the projectile material will survive (decreasing with increasing speed). If it were a 1 m diameter impactor, the mean fragment size would be 8–0.76 cm, distributed into between ~ 130 and 2400 fragments. This material will be distributed in, and beneath, the resulting impact crater. If the crater is subsequently eroded and sub-surface material exhumed, then the material could be present on the surface as the metal may be more resistant to erosion than the polar ice (or rocky surface in other regions). If we were to consider a larger impactor, one of size 15 m would produce fragments of mean in the size range 120–11 cm (impact speed of $5\text{--}10 \text{ km s}^{-1}$), which spans the size of iron meteorites (30–60 cm) reported on the martian surface by Fairen et al. (2011). The fragments will also be reasonably localised on scales of a few 10s of metres and will be paired, in that they will have a common origin and thus composition and age.

5. Summary

Hypervelocity impacts between different planetary bodies were common place in the early Solar System. Indeed once formed, bodies still undergo impacts whose mean speed is typically dependent on the location within the Solar System, falling to of order 1 km s^{-1} in the outer Solar System beyond Neptune (unless the impact occurs in the vicinity of a large planet with a contribution from the local in-fall speed). Investigating the composition of distinct craters on Solar System bodies can provide insights into the composition of impacting bodies which, in turn, can tell more about the comet's history. Previous work has found projectile material in craters on the Moon (Joy et al., 2012; Asphaug, 2013) and it is possible that missions such as *Stardust* may provide small samples of projectile material. Indeed, if *Rosetta* mission's *Philae* lander lands in an impact crater it may sample impactor material. For the *Deep Impact* mission, whose impactor was a metre scale body (contrasted to the mm scale here), the material beneath the crater will contain numerous small fragments of the impactor, some of which may also have been carried away from the impact crater as impact ejecta. In the examples here, a metallic impactor has been considered. However, if it were mineral in nature, as well

as being fragmented the material may have been altered by the impact, and various authors such as Bowden et al. (2008) and Parnell et al. (2010) for example, have shown that organic biomarkers in rocky projectiles in hypervelocity impacts are altered by the impact.

This study considered the survivability of copper impactors applied to specific examples such as the *Deep Impact* mission. If we ignore the complicated composition and internal structure of the impacting spacecraft and its non-solid copper mass, and simply consider a 1 m solid copper mass as the impactor, we predict that the recoverable fragments likely range in number from 500 to 10,000, in mean size from around 5 to 25 mm and comprise some 8–15% of the original copper mass. Further work to extend these results to more general impacts of other projectiles onto comet would involve the use of projectiles that are proxies for the most numerous material in the Solar System, namely chondritic, achondritic and metallic (Fe/Ni) projectiles. Such studies can also be applied to the possible survival of material from the *LCROSS* impact at the lunar south pole and iron bodies impacting Mars as meteorites.

Acknowledgments

We thank STFC for providing the funding to support this project. We thank the referees (K. Joy and an anonymous referee) for helpful comments which have improved the manuscript.

Appendix A. Further examples of recovered projectiles and their fragments

In this appendix we provide a set of images of projectile material after capture including examples already shown in the main text (see Figs. 1, 2 and 7). The images are arranged by increasing speed of impact. We provide two figures (Fig. A1: for 1 mm projectiles, and Fig. A2 for 2 mm projectiles). We provide images at three different scales: low resolution (to see material at the scale of the original projectile), intermediate resolution (to show several fragments together), and high resolution (to show detail on individual fragments).

References

- A'Hearn, M.F. et al., 2005. *Deep Impact: Excavating Comet Tempel 1*. Science 310 (5746), 258–264.
- Ahrens, T.J., Johnson, M.L., 1995. Shock wave data for minerals. In: Ahrens, T.J. (Ed.), *AGU Reference Shelf 2: Mineral Physics and Crystallography. A Handbook of Physical Constants*. American Geophysical Union, Washington, DC, pp. 143–184.
- Arvidson, R.E. et al., 2011. Opportunity Mars Rover mission: Overview and selected results from Purgatory ripple to traverses to Endeavour crater. *J. Geophys. Res.* 116. <http://dx.doi.org/10.1029/2010JE003746> E00F15.
- Asphaug, E., 2013. Go and catch a falling star. *Nat. Geosci.* 6, 422–423.
- Bland, P.A., Smith, T.B., 2000. Meteorite accumulations on Mars. *Icarus* 144, 21–26.
- Ben-Dor, G., Dubinsky, A., Elperin, T., 2010. Segmentation of high-speed/hypervelocity penetrators: Criteria of effectiveness based on approximate analytical models. *Mech. Des. Struct. Mach.* 38, 372–387.
- Bowden, S.A. et al., 2008. The thermal alteration by pyrolysis of the organic component of small projectiles of mudrock during capture at hypervelocity. *J. Anal. Appl. Pyrol.* 82, 312–314.
- Burchell, M.J., 2012. Cratering on icy bodies. In: Gudipati, M.S., Castillo-Rogez, J. (Eds.), *The Science of Solar System Ices*. Springer, pp. 253–278, 657 p. ISBN 978-1-4614-3075-9.
- Burchell, M.J., Johnson, E., 2005. Impact craters on small icy bodies, i.e. icy satellites and comet Nucleus. *Mon. Notices Roy. Astronom. Soc.* 360, 769–781.
- Burchell, M.J. et al., 1999. Hypervelocity impact studies using the 2 MV Van de Graaff accelerator and two-stage light gas gun of the University of Kent at Canterbury. *Meas. Sci. Technol.* 10 (1), 41–50.
- Burchell, M.J., Leliwa-Kopystyński, J., Arakawa, M., 2005. Cratering of icy targets by different impactors: Laboratory experiments and implications for cratering in the Solar System. *Icarus* 179, 274–288.

- Burchell, M.J. et al., 2009. Hypervelocity capture of particles in aerogel: Dependence on aerogel properties. *Planet. Space Sci.* 57, 58–70.
- Burchell, M.J. et al., 2012. Experimental investigation of impacts by solar cell secondary ejecta on silica aerogel and aluminium foil: Implications for the Stardust Interstellar Dust Collector. *Meteorit. Planet. Sci.* 47, 671–683.
- Burchell, M.J. et al., 2014a. Survival of organic materials in hypervelocity impacts of ice on sand, ice and water in the laboratory. *Astrobiology* 14 (6), 473–485.
- Burchell, M.J., McDermott, K.H., Price, M.C., 2014b. Survival of fossils under extreme shocks induced by hypervelocity impacts. *Philos. Trans. Roy. Soc. A* 372. <http://dx.doi.org/10.1098/rsta.2013.0190>.
- Daly, R.T., Schultz, P.H., 2013. Experimental studies into the survival and state of the projectile. *Lunar Plant. Sci.* XLIV. Abstract #2240.
- Daly, R.T., Schultz, P.H., 2014. How much of the impactor (and its water) ends up in Vesta's Regolith? *Lunar Plant. Sci.* XLV. Abstract #2070.
- Daly, R.T., Schultz, P.H., 2015. Predictions for impactor contamination on Ceres based on hypervelocity impact experiments. *J. Geophys. Res. Lett.* 42, 7890–7898.
- Davison, T.M., Collins, G.S., Ciesla, F.J., 2010. Numerical modelling of heating in porous planetesimal collisions. *Icarus* 208, 468–481.
- Dell'Oro, A. et al., 2001. Updated collisional probabilities of minor body populations. *Astron. Astrophys.* 366, 1053–1060.
- Ebert, M. et al., 2014. Geochemical processes between steel projectiles and silica-rich targets in hypervelocity impact experiments. *Geochim. Cosmochim. Acta* 133, 257–279.
- Ernst, C.A., Schultz, P.H., 2007. Evolution of the Deep Impact flash: Implications for the nucleus surface based on laboratory experiments. *Icarus* 190, 334–344.
- Fairen, A.G. et al., 2011. Meteorites at Meridiani Planum provide evidence for significant amounts of surface and near-surface water on early Mars. *Meteorit. Planet. Sci.* 46, 1832–1841.
- Fendyke, S., Price, M.C., Burchell, M.J., 2013. Hydrocode modelling of hypervelocity impacts on ice. *Adv. Space Res.* 52 (4), 705–714.
- Flynn, G.J., McKay, D.S., 1990. An assessment of the meteoritic contribution to the martian soil. *J. Geophys. Res.* 95, 14497–14509.
- Goderis, S., Paquay, F., Claeys, P., 2013. Projectile identification in terrestrial impact structures and ejecta material. In: Osinski, G.R., Pierazzo, E. (Eds.), *Impact Cratering Processes and Products*. Wiley-Blackwell, pp. 223–239, ISBN 978-1-4051-9829-5 (Chapter 15).
- Gounelle, M. et al., 2003. Mineralogy of carbonaceous chondritic microclasts in howardites: Identification of C2 fossil micrometeorites. *Geochim. Cosmochim. Acta* 67, 507–527.
- Hayhurst, C.J., Clegg, R.A., 1997. Cylindrically symmetric SPH simulations of hypervelocity impacts on thin plates. *Int. J. Impact Eng.* 20 (1–5), 337–348.
- Hermalyn, B. et al., 2012. Scouring the surface: Ejecta dynamics and the LCROSS impact event. *Icarus* 218, 654–665.
- Hernandez, V.S., Murr, L.E., Anchondo, I.A., 2006. Experimental observations and computer simulations for metallic projectile fragmentation and impact crater development in thick metal targets. *Int. J. Impact Eng.* 32, 1981–1999.
- Joy, K.H. et al., 2012. Direct detection of projectile relics from the end of the lunar basin-forming epoch. *Science* 336 (6087), 1426–1429.
- Kenkmann, T. et al., 2013. Deformation and melting of steel projectiles in hypervelocity cratering experiments. *Meteorit. Planet. Sci.* 48 (1), 150–164.
- Lee, W.S. et al., 2011. Dynamic mechanical response of biomedical 316L stainless steel as function of strain rate and temperature. *Bioinorg. Chem. Appl.* 2011, 13. <http://dx.doi.org/10.1155/2011/173782>.
- Le Feuvre, M., Wieczorek, M.A., 2011. Nonuniform cratering of the Moon and a revised crater chronology of the inner Solar System. *Icarus* 214, 1–20.
- Marshall, W. et al., 2012. Locating the LCROSS impact craters. *Space Sci. Rev.* 167, 71–92.
- Melosh, H.J., 1989. *Impact Cratering: A Geologic Process*. Oxford University Press, Oxford, UK.
- Nagaoka, Hiroki. et al., 2014. Degree of impactor fragmentation under collision with a regolith surface—Laboratory impact experiments of rock projectiles. *Meteorit. Planet. Sci.* 49 (1), 69–79.
- Parnell, J. et al., 2010. The preservation of fossil biomarkers during hypervelocity impact experiments using organic rich siltstones as both projectiles and targets. *Meteorit. Planet. Sci.* 45, 1340–1358.
- Piekutowski, A.J., 1995. Fragmentation of a sphere initiated by hypervelocity impact with a thin sheet. *Int. J. Impact Eng.* 17 (4), 627–638.
- Pierazzo, E., Melosh, H.J., 2000. Hydrocode modelling of oblique impacts: The fate of the projectile. *Meteorit. Planet. Sci.* 35, 117–130.
- Pierazzo, E. et al., 2008. Validation of numerical codes for impact and explosion cratering: Impacts on strengthless and metal targets. *Meteorit. Planet. Sci.* 43 (12), 1917–1938.
- Potter, R.W.K., Collins, G.S., 2013. Numerical modeling of asteroid survivability and possible scenarios for the Morokweng crater-forming impact. *Meteorit. Planet. Sci.* 48 (5), 744–757.
- Price, M.C., Kearsley, A.T., Burchell, M.J., 2013. Validation of the Preston-Tonks-Wallace strength model at strain rates of 10^{13} s^{-1} for Al-1100, tantalum and copper using hypervelocity impact crater morphologies. *Int. J. Impact Eng.* 52, 1–10.
- Reddy, V. et al., 2012. Delivery of dark material to Vesta via carbonaceous chondritic impacts. *Icarus* 221 (2), 544–559.
- Richardson, J.E., Melosh, H.J., 2013. An examination of the Deep Impact collision site on Comet Tempel 1 via Stardust-NExT: Placing further constraints on cometary surface properties. *Icarus* 222, 492–501.
- Richardson, J.E. et al., 2007. A ballistics analysis of the Deep Impact ejecta plume: Determining Comet Tempel 1's gravity, mass, and density. *Icarus* 191, 176–209.
- Schultz, P.H., Crawford, D., 2014. Lunar basin-forming projectiles. *Lunar Plant. Sci.* XLV. Abstract #1691.
- Schultz, P.H., Gault, D.E., 1984. Effects of projectile deformation on crater efficiency and morphology. *Lunar Plant. Sci.* XV. Abstract #730.
- Schultz, P.H., Gault, D.E., 1990. Prolonged global catastrophes from oblique impacts. In: Sharpton, V.L., Ward, P.D. (Eds.), *Global Catastrophes in Earth History; an Interdisciplinary Conference on Impacts, Volcanism, and Mass Mortality*. Geological Society of America Special Paper 247, pp. 239–261.
- Schultz, P.H. et al., 2007. The Deep Impact oblique impact cratering experiment. *Icarus* 190, 295–333.
- Schultz, P.H. et al., 2010. The LCROSS cratering experiment. *Science* 330 (6003), 468–472.
- Schultz, P.H., Hermalyn, B., Veverka, J., 2013. The Deep Impact crater on 9P/Tempel-1 from Stardust-NExT. *Icarus* 222, 502–515.
- Senft, L.E., Stewart, S., 2008. Modeling the morphological diversity of impact craters on icy satellites. *Meteorit. Planet. Sci.* 43, 1993–2013.
- Steinberg, D.J., 1991. *Equation of State and Strength Properties of Selected Materials*. Lawrence Livermore National Laboratory, UCRL-MA-106439 (re-issued 1996).
- Steinberg, D.J., Cochran, S.G., Guinan, M.W., 1980. A constitutive model for metals applicable at high strain rates. *J. Appl. Phys.* 51 (3), 1498–1504.
- Veverka, J. et al., 2013. Return to Comet Tempel 1: Overview of Stardust-NExT results. *Icarus* 222, 424–435.
- Yue, Z. et al., 2013. Projectile remnants in central peaks of lunar impact craters. *Nat. Geosci.* 6, 435–437.
- Zahnle, K. et al., 2003. Cratering rates in the outer Solar System. *Icarus* 163, 263–289.
- Zolensky, M.E. et al., 1996. Mineralogy of carbonaceous chondrite clasts in howardites, eucrites and the Moon. *Meteorit. Planet. Sci.* 31, 518–537.